ELSEVIER

Remote Sensing of Environment 82 (2002) 335–348

Remote Sensing of Environment

www.elsevier.com/locate/rse

Characterization of forest types in Northeastern China, using multi-temporal SPOT-4 VEGETATION sensor data

Xiangming Xiao [a,*], Stephen Boles [a], Jiyuan Liu [b], Dafang Zhuang [b], Mingliang Liu [b]

[a] *Institute for the Study of Earth, Oceans and Space, University of New Hampshire, Durham, NH 03824, USA*
[b] *Institute of Geographical Sciences and Natural Resources, Chinese Academy of Sciences, Beijing 100101, China*

Received 27 December 2001; received in revised form 15 April 2002; accepted 20 April 2002

Abstract

In this study, we explored the potential of multi-temporal SPOT-4 VEGETATION (VGT) sensor data for characterization of temperate and boreal forests in Northeastern China. As the VGT sensor has a short-wave infrared (SWIR) band that is sensitive to vegetation, soil moisture and leaf water content, the Normalized Difference Water Index (NDWI) was calculated in addition to the Normalized Difference Vegetation Index (NDVI). A forest map of Northeast China was generated from an unsupervised classification of 25 10-day VGT composite data (NDVI and NDWI) over the period of March 11–20, 1999 to November 11–20, 1999. Seven different forest categories were distinguished from the 1-km spatial resolution VGT data. The VGT forest map was compared to estimates of forest area derived from Landsat 7 Enhanced Thematic Mapper (ETM+) images. There was a good agreement on spatial distribution and area of forest between the VGT product and the TM product, however, the VGT product provided additional information on forest type. Analysis of NDVI and NDWI over the plant growing season allows for the identification of distinct growth patterns between the different forest types. It is evident that VGT data can be used to provide timely and detailed forest maps with limited ancillary data needed. The VGT-derived forest maps could be very useful as input to biogeochemical models (particularly carbon cycle models) that require timely estimates of forest area and type.

1. Introduction

Northeastern China (Fig. 1) has abundant tree species and a variety of forest types, including evergreen needleleaf forest, deciduous needleleaf forest, deciduous broadleaf forest, and mixed forests (Zheng, Xiao, Guo, & Howard, 2001). Human activities (e.g. forest clear-cutting, selective logging, agricultural encroachment) and natural disturbance (e.g. fire, insects) have resulted in substantial losses of the old-growth forests and fragmentation in forest landscapes (Shao et al., 1996; Chen, 2000; Chen, Zhang, Zhou, & Chen, 2000; Liu, Kondoh, Tateishi, Takamura, & Takeuchi, 2001; Wang, Feng, & Ouyang, 2001). For instance, most of the mixed broadleaf/Korean pine (*Pinus koraiensis*) forests in Jilin and Liaoning Provinces have been replaced (plantation-style) by faster-growing species such as larch (*Larix* sp.), poplar (*Populus* sp.) and birch (*Betula* sp.) (Jiang et al., 1999). Fang, Chen, Peng, Zhao, and Ci (2001) and Fang, Wang, Liu, and Xu (1998) have shown that there is considerable spatial variability in biomass carbon storage and density among forest types in China. For example, the larch forests of Northeast China tend to have higher carbon densities than the oak forests (Fang et al., 1998; Jiang, Peng et al., 1999). Recent carbon cycle studies have indicated that the mid- to high-latitude forests of the Northern Hemisphere may serve as a significant carbon sink (Schimel et al., 2001).

Timely and accurate information on forest types and areas at the regional scale is needed for natural resource management, carbon cycle studies and modeling of biogeochemistry, hydrology and climate. Satellite-based remote sensing products provide one option to meet those data needs. A number of earlier studies have used Landsat Thematic Mapper (TM) images to document forest types and changes at Changbai Mountain, Jilin Province, where an International Biosphere Reserve was established in 1979 (Shao et al., 1996; Zheng, Wallin, & Hao, 1997; Liu, Kondoh et al., 2001). Because of frequent cloud cover and the long re-visit time (16 days) of Landsat, it is difficult to acquire cloud-free images for monitoring the changes in forest types at short-term intervals (e.g. yearly). Over the last two decades, numerous studies of large-scale mapping of land cover and land use have explored data

* Corresponding author. Tel.: +1-603-862-3818; fax: +1-603-862-0188.
E-mail address: xiangming.xiao@unh.edu (X. Xiao).

0034-4257/02/$ - see front matter © 2002 Published by Elsevier Science Inc.
PII: S0034-4257(02)00051-2

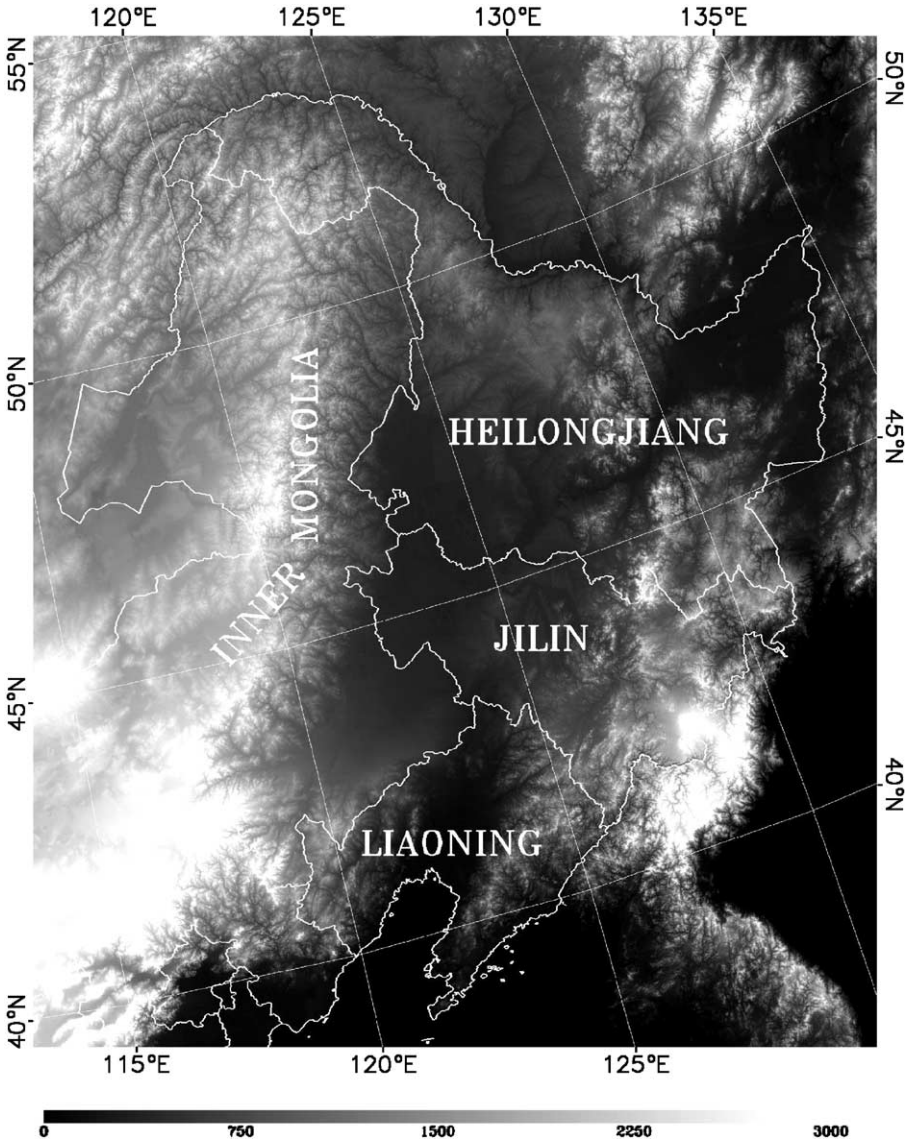

Fig. 1. The elevation map of the study area that includes portions of China, Russia, Mongolia and the Korean Peninsula. The polygon map is the provincial boundary map of China. The background is the Global Land One-Kilometer Base Elevation dataset (http://www.ngdc.noaaa.gov).

from the Advanced Very High Resolution Radiometer (AVHRR) sensors that provide daily observations of the Earth at 1- and 4-km spatial resolutions (Tucker, Townshend, & Goff, 1985; Goward, Tucker, & Dye, 1985; Loveland, Merchant, & Brown, 1991; Loveland et al., 2000; Zhu & Evans, 1994; Stone, Schlesinger, Houghton, & Woodwell, 1994; Defries, Hansen, & Townshend, 1995; Hansen, DeFries, Townshend, & Sohlberg, 2000; Liu, Zhuang, Lou, & Xiao, 2001). Multi-temporal AVHRR have also been used to map forest types in northeastern China (Liu, Zhuang, & Ling, 1998). However, the AVHRR sensors, originally designed for meteorological applications, have only two spectral channels (red and near infrared) that are related to vegetation and phenology. Recently, a new generation of space-borne optical sensors designed for studying vegetation and land surfaces have been launched, i.e. the VEGETATION (VGT) sensor onboard the SPOT-4 satellite and the Moderate Resolution Imaging Spectroradiometer (MODIS) onboard the Terra (EOS AM-1) satellite. VGT and MODIS sensors have a number of advantages over AVHRR, including more spectral bands that are related to vegetation (see Section 2 for more details about the VGT sensor). Multi-temporal VGT data have been used in the mapping of tropical forests (Mayaux, Gond, & Bartholome, 2000), agriculture in China (Xiao et al., in press(a), in press(b)) and alpine snow and ice cover in Asia (Xiao, Moore, Qin, Shen, & Boles, 2002; Xiao, Shen, & Qin, 2001).

In this study, we explored the potential of multi-temporal VGT data for mapping of various forest types in Northeastern China. The objective was twofold: (1) to document the current status of forest types and areas in

northeastern China, using VGT data acquired in 1999; and (2) to evaluate the potential of VGT data in identifying various types of forests. The forests of Northeastern China are similar to those of the Great Lakes region of North America (Burger & Zhao, 1988; Barnes, Xu, & Zhao, 1992; Geng, Pastor, & Dewey, 1993), therefore, this study would also help the efforts in mapping forests in North America using VGT data, as part of the goal of global mapping of forests. In addition, the resultant forest map derived from this VGT image analysis can be used to improve estimates of forest biomass and carbon storage in Northeastern China, and to initialize simulations of primary productivity models that require estimates of forest type distribution (Jiang, Apps, Zhang, Peng, & Woodard, 1999; Jiang, Peng et al., 1999).

2. VEGETATION image data and pre-processing

The VGT instrument is one of a new generation of space-borne optical sensors that were designed for observations of vegetation and land surfaces (Saint, 2000). The VGT instrument has four spectral bands: B0 (blue, 430–470 nm), B2 (red, 610–680 nm), B3 (near infrared, 780–890 nm) and SWIR (short-wave infrared, 1580–1750 nm), which are equivalent to Landsat Thematic Mapper (TM) bands 1, 3, 4, and 5, respectively. The blue band is primarily used for atmospheric correction. The SWIR band is sensitive to soil moisture, vegetation cover and leaf moisture content, and can improve the discrimination of vegetation and other land covers. With a swath width of 2250 km, VGT provides daily coverage of the globe at 1-km spatial resolution. Unlike scanner sensors (e.g. AVHRR), the VGT instrument uses the linear-array technology and thus produces high-quality imagery at coarse resolution with greatly reduced distortion. The SPOT-4 satellite carries both the VGT sensor and High Resolution Visible and Infrared sensor (HRVIR); both of them use the same geometric reference system and identical spectral bands to facilitate multi-scale interpretation.

Three standard VGT products are available to users: VGT-P (physical product), VGT-S1 (daily synthesis product) and VGT-S10 (10-day synthesis product). The spectral bands in the VGT-S1 products are estimates of ground surface reflectance, as atmospheric corrections for ozone, aerosols and water vapor have been applied to the VGT-P images using the simplified method for atmospheric correction algorithm (Rahman & Dedieu, 1994). There are three 10-day composites for 1 month: days 1–10, days 11–20, and day 21 to the last day of the month. VGT-S10 data are generated by selecting the VGT-S1 pixels that have the maximum Normalized Difference Vegetation Index (NDVI) values within a 10-day period. The maximum NDVI value composite (MVC) approach helps minimize the effect of cloud cover and variability in atmospheric optical depth. Fig. 2 includes three examples of VGT-S10 products, which illustrate the ability of VGT-S10 data to sense the development of the seasonal phenology of vegetation in northeastern China. Twenty-seven VGT-S10 composites for the period of March 1–10, 1999 to November 21–30, 1999 were acquired and subset for a study area of 1500 by 1800 km^2 (Fig. 1).

Tucker (1980) suggested that the short-wave infrared band (TM5) of Landsat TM was best suited for remote sensing of plant canopy water content. Gao (1996) and Jürgens (1997) proposed sensor-specific Normalized Difference Water Index (NDWI) for remote sensing of vegetation liquid water, using near-infrared and short-wave infrared reflectance values. In this study, both NDWI and NDVI were calculated for each of the VGT-S10 products, using the following equations:

$$\mathrm{NDWI}_{\mathrm{VGT}} = (\mathrm{B3} - \mathrm{SWIR})/(\mathrm{B3} + \mathrm{SWIR}) \quad (1)$$

$$\mathrm{NDVI}_{\mathrm{VGT}} = (\mathrm{B3} - \mathrm{B2})/(\mathrm{B3} + \mathrm{B2}) \quad (2)$$

Both NDVI and NDWI values are within a range of −1.0–1.0. For reduction of file sizes, the resultant floating-point NDVI and NDWI values were rescaled to eight-bit digital numbers between 3 and 253, using the same scaling method developed by the NASA Pathfinder AVHRR Land Project (PAL) for AVHRR-derived NDVI data from 1981 to 2000 (http://daac.gsfc.nasa.gov/CAMPAIGN_DOCS/FTP_SITE/readmes/pal.html).

Although the MVC procedure eliminates most cloudy pixels, some VGT-S10 products contain residual cloud contamination that could adversely affect our analysis. One approach to further reduce cloud cover in images is to generate monthly composites of images by selecting those pixels that have the maximum NDVI values within a month. However, the resultant monthly composites might not resolve large and fast changes in the temporal development of vegetation greenness (e.g. green-up, senescence). To facilitate interpretation of vegetation types, the original 10-day temporal resolution of the dataset needs to be kept. We decided to identify and smooth those VGT-S10 pixels that have clouds, using neighboring pixels in the time-series data. The VGT-S10 product provides a status map file for all pixels, including radiometric quality, clouds, snow/ice and land/ocean. The first step of pre-processing uses the cloud flag in the status map file. For pixel i at time t, if it is described as a cloud pixel in the status map, we will use one cloud-free pixel before time t (in most cases $t-1$) and one cloud-free pixel after time t (in most cases $t+1$) to calculate the average NDVI and NDWI values, and replace those values at time t for pixel i. However, the cloud detection algorithm used in producing the standard VGT products does not detect all cloud cover, as illustrated by sudden decreases of NDVI prior to senescence (Fig. 3a). Earlier studies had developed the Best Index Slope Extraction (BISE) technique for reducing the effects of cloud contamination and atmospheric interference in seasonal NDVI time

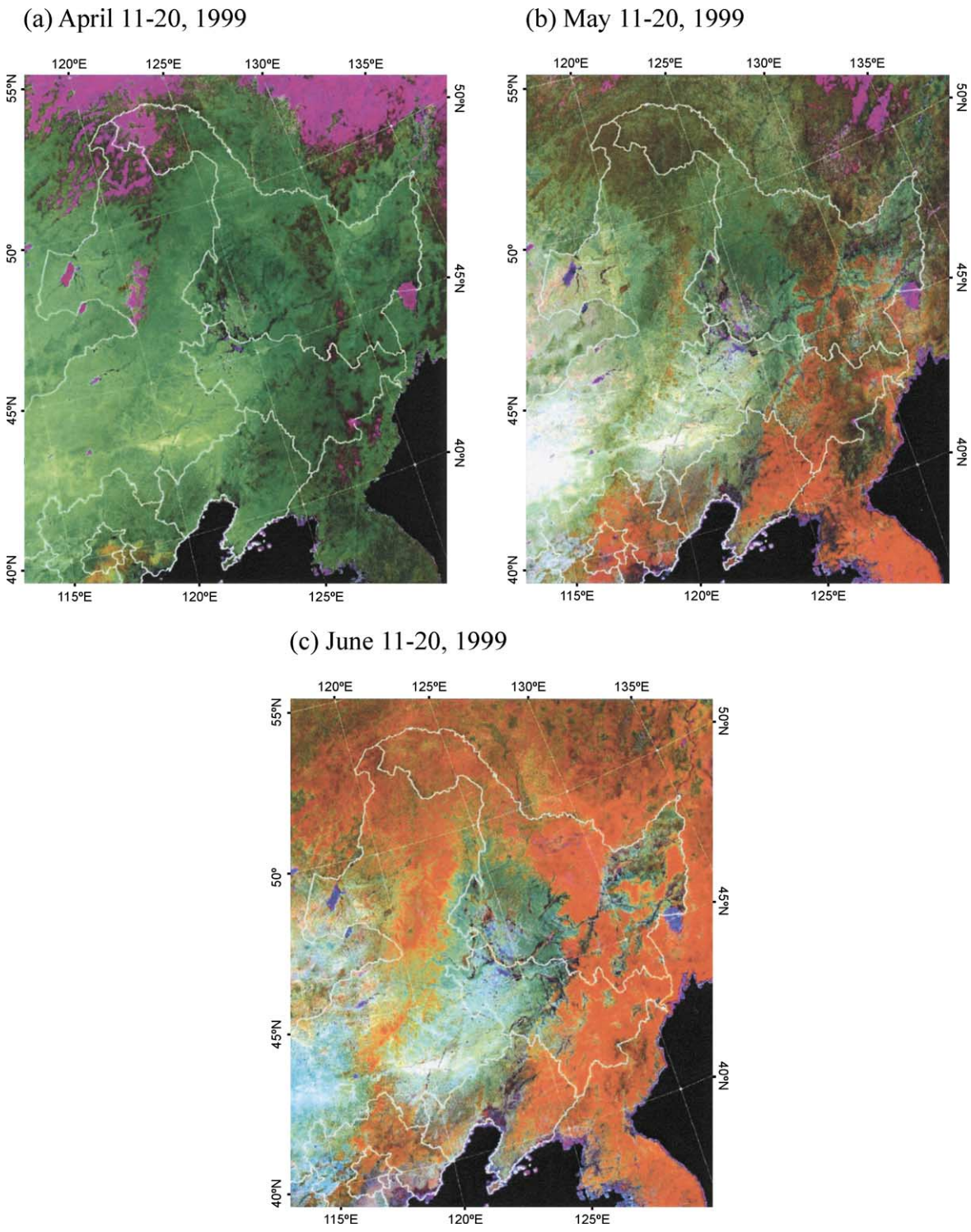

Fig. 2. Seasonal phenology of vegetation in northeastern China as illustrated by three 10-day VGT composites in 1999. Each image is a false color composite of spectral bands: near infrared (B3), short-wave infrared (SWIR) and red (B2).

series from daily AVHRR data (White, Thornton, & Running, 1997; Reed et al., 1994; Viovy, Arino, & Belward, 1992). The BISE algorithm contains two main assumptions: (1) NDVI is depressed by cloud and atmospheric contamination, and (2) rapid and non-persistent increases or decreases in NDVI are inconsistent with natural vegetation growth. In this study, the second step of pre-processing for removal of residual cloud cover is to examine NDVI values at three time steps: $t-1$, t, and $t+1$. We calculated the difference in NDVI values between time $t-1$ and time t,

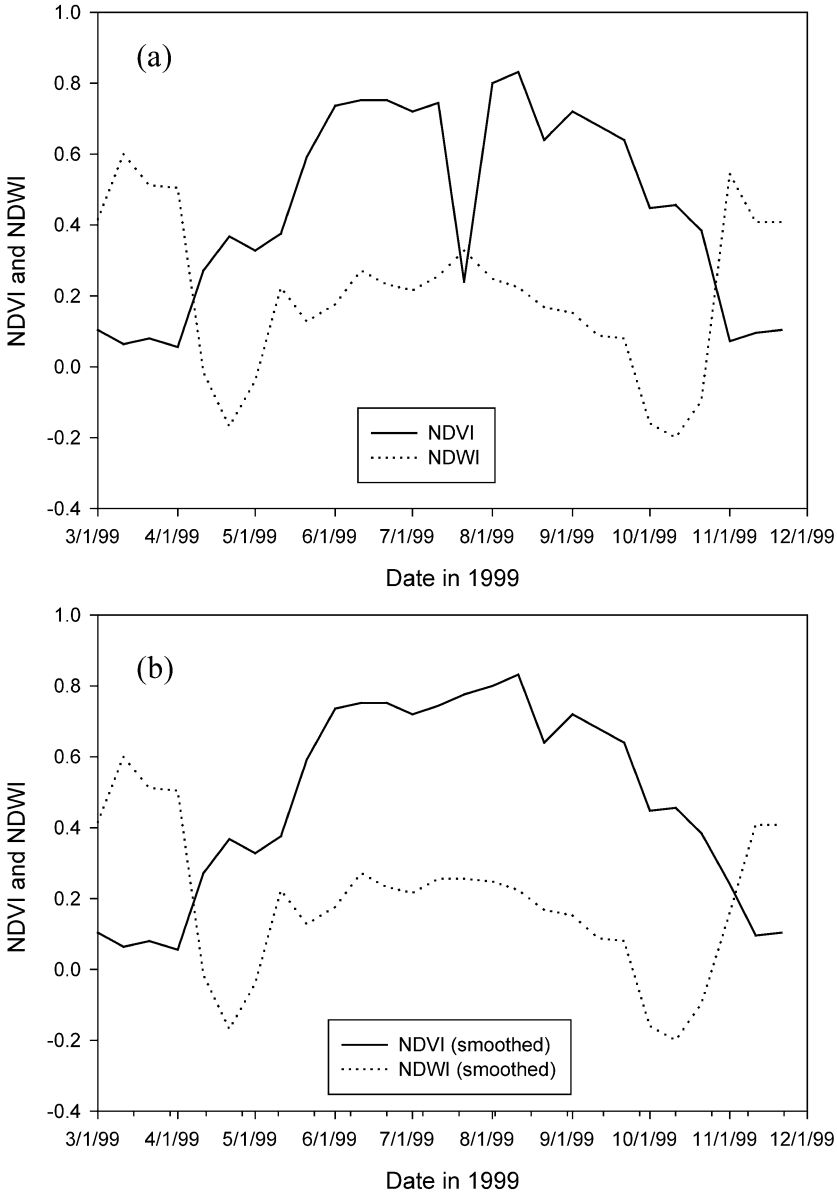

Fig. 3. Time series of NDVI and NDWI of a VGT forest pixel over the period of March 1–10 to November 21–30, 1999. (a) Before applying the smoothing algorithm; (b) after applying the smoothing algorithm.

and the difference in NDVI between time $t+1$ and t, respectively:

$$d\mathrm{NDVI}_{t-1,t} = (\mathrm{NDVI}_{t-1} - \mathrm{NDVI}_t) \quad (3)$$

$$d\mathrm{NDVI}_{t,t+1} = (\mathrm{NDVI}_{t+1} - \mathrm{NDVI}_t) \quad (4)$$

Adopting the method proposed by White et al. (1997), a threshold of 20% decline in the NDVI value at time t was adopted for identifying cloudy pixels. If $d\mathrm{NDVI}_{t-1,t}$ and $d\mathrm{NDVI}_{t,t+1}$ were at least a 20% decline from both NDVI_{t-1} and NDVI_{t+1}, respectively, it is assumed that the pixel was affected by clouds. In these instances, NDVI_t and NDWI_t values were replaced by the averaged NDVI and NDWI values at time $t-1$ and time $t+1$, respectively. We applied the algorithm to smooth the NDVI and NDWI time-series data over the period of March 11–20, 1999 to November 11–20, 1999 (a total of 25 time periods; Fig. 3b). The NDVI and NDWI data for the periods of March 1–10 and November 21–30 are the starting and ending points in the time series and therefore were not corrected and not used for image classification.

3. Method

3.1. Classification and interpretation

There are two general approaches for land cover classification: per-pixel binary (0 or 1) and sub-pixel unmixing (percentage fractional cover within a pixel). Per-pixel binary

approach is the most widely used method, including the International Geosphere–Biosphere Programme (IGBP) Global Land Cover Data dataset (DIScover) that was derived from 1-km AVHRR data in 1992/1993 (Loveland et al., 2000). In this study, we explored the potential and limitations of the per-pixel binary approach using coarse-resolution VGT data and fine-resolution land cover products derived from Landsat images. The unsupervised classification procedure (ISODATA) was used for image classification, as it allows for the identification of all the important spectral groupings without initially knowing which are thematically significant (Cihlar et al., 1998). NDVI and NDWI bands from March 11–20, 1999 to November 11–20, 1999 (a total of 50 bands) were used as input to the iterative ISODATA clustering algorithm. Forty spectral clusters were generated with the following parameters: convergence threshold (95%), maximum number of merge pairs (2), minimum class standard deviation (1), minimum number of pixels in a class (100), and maximum number of iterations (10).

The hierarchical forest classification scheme is based on leaf life-form (needleleaf and broadleaf) and leaf longevity (evergreen and deciduous), and thus has the following categories for the study area: evergreen needleleaf forest, deciduous needleleaf forest, deciduous broadleaf forest, and various mixed forests. For each of the forest categories, identification of dominant tree species is required. To aid in interpretation and labeling of the 40 spectral clusters, a number of ancillary datasets were used, including the 1:1,000,000 Land Use Map of China (Wu, 1990), the Atlas of Forestry in China (The Editorial Committee for the Atlas of Forestry in China [ECAFC], 1990), and the Forests of China (Wang, 1961). The Land Use Map of China has four different forest classes in northeastern China (coniferous, broadleaf, mixed, oak). The Atlas of Forestry in China provides maps of forests and forest industry by province. Wang (1961) described the boreal and temperate forests of northeastern China and provided detailed descriptions of the forest communities that exist, including tree species, understory vegetation, and plant communities of the forest floors.

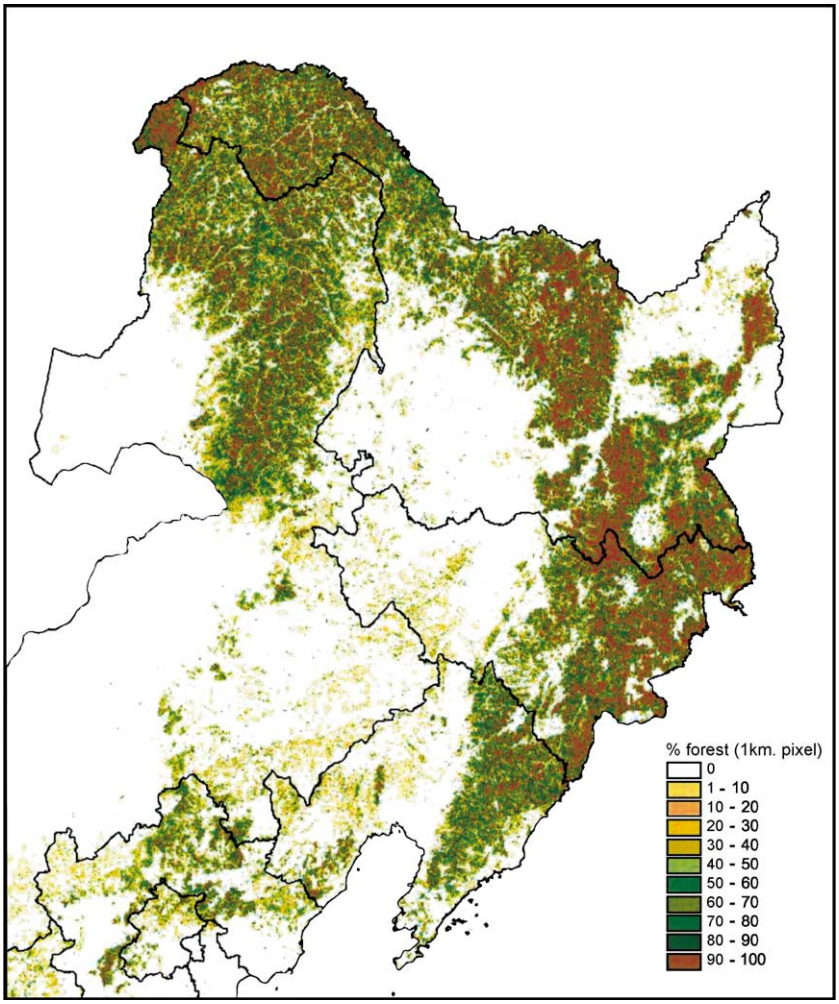

Fig. 4. The spatial distribution of forest in northeastern China according to the National Land Cover Dataset (NLCD) that was derived from Landsat 7 ETM+ images in 1999 and 2000. The legend is percent fractional cover of forest within 1-km pixels in northeastern China.

Vegetation distribution is related to elevation gradients, therefore, we downloaded the Global Land One-Kilometer Base Elevation dataset at the NOAA National Geophysical Data Center (http://www.ngdc.noaa.gov/) and subset it for the study area (Fig. 1). The digital elevation model was used as an aid for interpretation and labeling of the spectral clusters. In addition, summary statistics (e.g. mean, minimum, maximum, standard deviation) of all the NDVI and NDWI bands for individual spectral clusters were calculated and compared for characterization of temporal NDVI and NDWI dynamics of the 40 spectral clusters. A data matrix of mean NDVI and NDWI values for the 40 spectral clusters (50 bands × 40 clusters) was also constructed, and a dendrogram was generated as an additional aid for cluster interpretation and labeling.

3.2. Accuracy assessment

Accuracy assessment for coarse-resolution (e.g. 1 km) land cover maps poses a great challenge to the remote sensing community, as the 1-km maps overestimate or underestimate forest areas according to forest fragmentation and proportion (Mayaux & Lambin, 1997; Achard, Eva, & Mayaux, 2001). As an alternative approach to field surveys, fine-resolution images and derived land cover maps have been used for validation of thematic maps. For example, to validate the IGBP DISCover dataset, a sample of Landsat TM and SPOT HRV images were used (Scepan, 1999; Scepan, Menz, & Hansen, 1999). In this study, although VGT images cover portions of China, Russia, Mongolia, North Korea and South Korea (Fig. 1), accuracy assessment was restricted to China as we only had a detailed and consistent dataset to support validation within China.

Recently, the National Land Cover Project (supported by the Chinese Academy of Sciences) completed the analysis of Landsat 7 Enhanced Thematic Mapper (ETM+) images acquired in 1999 and 2000 for China. Hundreds of ETM+ images were geo-referenced and ortho-rectified, using field-collected ground control points and fine-resolution digital elevation models. A classification system of 25 land cover types was used in the project, including a 'forest' category defined as natural or planted forests with a canopy cover of greater than 30%. Visual interpretation and digitalization of ETM+ images were conducted to generate a thematic map of land use and land cover in China at a scale of 1:100,000. The resultant vector National Land Cover Dataset (NLCD-1999/2000) was converted into a gridded database at 1-km resolution. The unique feature of this 25-layer gridded 1-km database is that it still captures all of the land cover information at the 1:100,000 scale by calculating percent fractional cover within a 1-km pixel for individual land cover types (Tang, 2000). Fig. 4 shows the spatial distribution of percent forests cover within 1-km pixels in northeastern China, according to the NLCD-1999/2000 dataset. In this study, the 1-km resolution gridded 'forest' layer of the NLCD dataset was used for accuracy assessment of the VGT-based image classification.

4. Results

4.1. Forest classification map

Northeast China is home to a very diverse collection of forest types, ranging from temperate broadleaf forests in the south to boreal coniferous forests in the north. The forests are widely distributed over mountainous terrain (e.g. Daxinganling and Xiaoxinganling Ranges), and have large variations in species composition across latitudinal domains, elevation gradients, and moisture gradients (Burger & Zhao, 1988; Barnes et al., 1992; Geng et al., 1993; Richardson, 1990). At low elevation, dominant tree species include Korean pine (*P. koraiensis* Sied. & Zucc), five-needled white pine (*P. strobes* L.), basswood (*Tilia amurensis* Rupr.), white oak (*Quercus mongolica* Fishc. & Turz.), painted maple (*Acer mono* Maxim.), and ash (*Fraxinus mandshurica* L.). At high elevation, major tree species include spruce (*Picea Koraiensis* Nakai), fir (*Abies nephrolepsis* (Trautv.) Maxim), pine (*P. sylvestris var.mongolica*), aspen (*Populus davidiana* Dode.), and birch (*Betula platyphylla* Suk.). Deciduous coniferous *Larix* forests, which are widely distributed in the most northern part of the Northeastern China, include *Larix gmelinii, L. dahurica* Turcz. and *L. olgensis* A. Henry.

In the VGT image classification, seven forest types were identified and mapped for the study region (Fig. 5): deciduous needleleaf forest (DN), evergreen needleleaf forest (EN), three types of deciduous broadleaf forest (DB) and two types of mixed forests (DN/DB, and EN/DB). The deciduous needleleaf forest, dominated by larch trees, has an area of 216,785 pixels and is widely distributed in the far north. Evergreen needleleaf forest, dominated by spruce, fir and pine, has an area of 53,239 pixels and is largely distributed in the northeastern part of the study area and in mountainous areas. Oak-dominated deciduous broadleaf forest (DB-o; 48,692 pixels) is largely distributed in the south, while maple–birch–basswood-dominated broadleaf forest (DB-m–b–b; 308,891 pixels) is widely distributed in the eastern part of the study area. Birch-dominated deciduous broadleaf forest (DB-b; 179,089 pixels) occurs mostly in the northern Daxinganling Range. Evergreen needleleaf and deciduous broadleaf mixed forest (EN/DB; 124,879 pixels) is largely distributed in the eastern part of the study area within an elevation gradient zone that is above deciduous broadleaf forest but below evergreen needleleaf forest (Fig. 5). In comparison, deciduous needleleaf and deciduous broadleaf mixed forest (DN/DB; 107,886 pixels) is largely concentrated in the northwestern part of the study area, where elevation is at an intermediate level and fire events occur frequently. According to the VGT-derived forest map, the total number of pixels for the entire study region is estimated to be 1,039,461 Fig. 5).

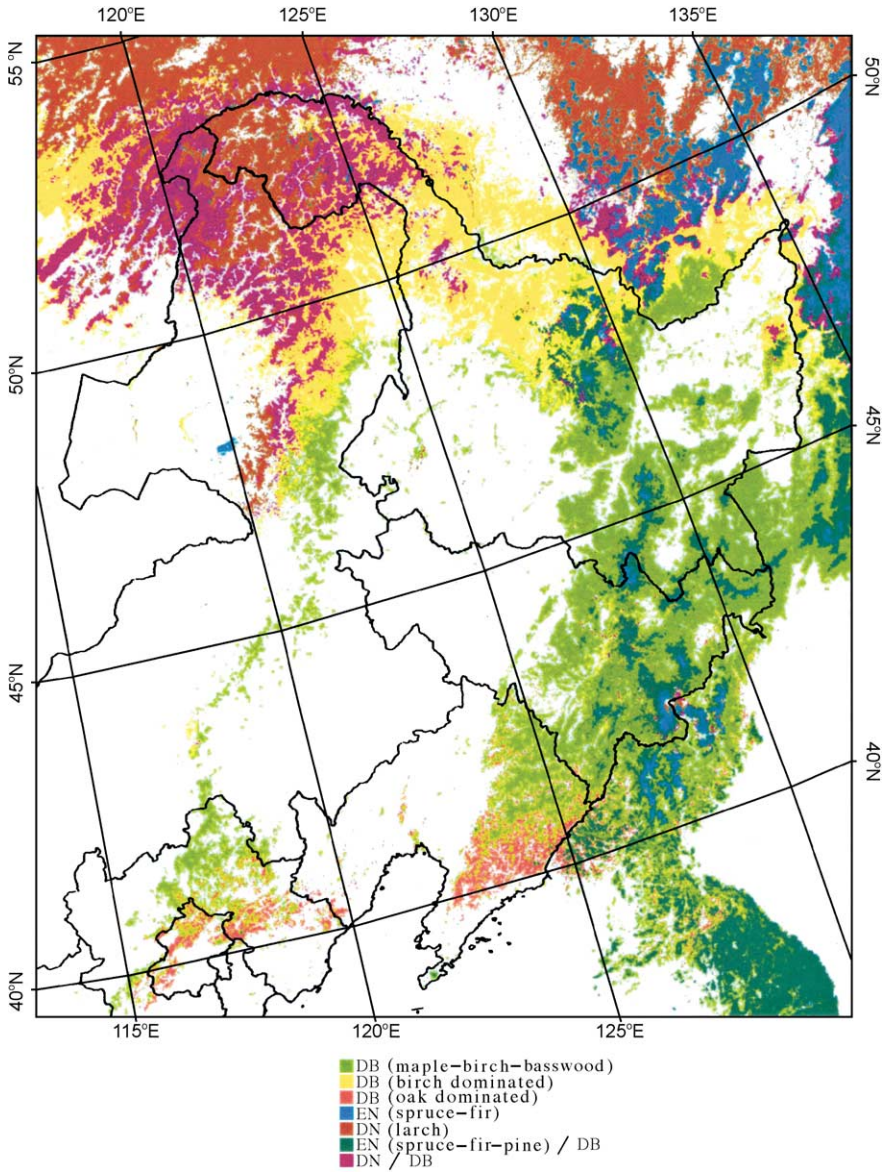

Fig. 5. Forest classification map derived from multi-temporal VGT-S10 images in 1999.

Aggregation and reporting of remote sensing products at 1-km resolution to the administrative units (e.g. provincial level) allows comparison with Chinese forest inventory data (Ministry of Forestry, 1990, 1996). Using a geographical information system, the provincial boundary map of China was overlaid with the VGT-derived forest map and the numbers of forest pixels within individual provinces were counted. Table 1 summarizes the numbers of forest pixels in the four provinces (Inner Mongolia, Heilongjiang, Jilin and Liaoning) of the northeastern China. According to the VGT-derived forest map, Heilongjiang has the largest number of forest pixels (212,930), while Liaoning has the smallest number of forest pixels (45,715). The sum of forest pixels for these four provinces is 478,287 (Table 1). In the conventional per-pixel binary (0 or 1) approach, a pixel is assumed to be 100% forest area if it is classified as forest. Using that approach, the VGT-derived forest map has a total forest area of 478,287 km^2 in these four provinces (Table 1). Table 1 lists the provincial-level estimates of forest area from the 4th forest inventory during the period of 1989–1993, which was organized and conducted by the Ministry of Forestry, China (Ministry of Forestry, 1990, 1996; Zheng et al., 2001). The total forest area (404,932 km^2) of the four provinces from the forest inventory data over the period of 1989–1993 is about 18% lower than the VGT-derived estimate of the forest area (478,287 km^2). The provincial boundary map was also overlaid with the NLCD-1999/2000 dataset at 1-km resolution. It is estimated that these four provinces together have a total forest area 401,746

Table 1
Provincial-level estimates of forest area (km^2) from the VGT analysis, NLCD-1999/2000, and forest statistics in 1993

Forest type	Inner Mongolia	Heilongjiang	Jilin	Liaoning	Total
Evergreen needleleaf (EN)	618	2098	1914	2	4632
Deciduous needleleaf (DN)	27,161	27,160	486	43	54,850
Deciduous broadleaf (DB-b)	44,768	57,836	2022	89	104,715
Deciduous broadleaf (DB-m–b–b)	21,260	81,587	67,143	24,334	194,324
Deciduous broadleaf (DB-o)	107	28	1610	20,950	22,695
Mixed (EN/DB)	57	22,551	17,207	270	40,085
Mixed (DN/DB)	34,278	21,670	1011	27	56,986
Total VGT forest area (per-pixel estimate)	128,249	212,930	91,393	45,715	478,287
Total NLCD forest area	116,112	175,742	71,191	38,701	401,746
Total NFRS forest area	140,657	161,620	63,469	39,186	404,932

km^2 from the NLCD-1999/2000 dataset, which is approximately 19% lower than the VGT-derived estimate of forest area.

4.2. Accuracy assessment at pixel level for Northeastern China

In the NLCD-1999/2000 dataset, there are 654,373 pixels (1-km^2) that have 1% or more fractional cover of forest, resulting in a total forest area of 423,332 km^2 for the Chinese portion of the study area (Fig. 4). The frequency distribution of those NLCD pixels is skewed to the right (Fig. 6). About 77% of the NLCD pixels has a fractional forest cover of 30% or more within a 1-km pixel, accounting for 95% of the total forest area. About 60% of the NLCD pixels has a fractional forest cover of 60% or more within a 1-km pixel, accounting for 83% of the total forest area.

In the VGT-derived forest map, there are 508,621 forest pixels in the Chinese portion of the study area: 4632 pixels of evergreen needleleaf forest, 54,850 pixels of deciduous needleleaf forest, 104,725 pixels of birch-dominated deciduous broadleaf forest, 211,336 pixels of maple–birch–basswood dominated deciduous broadleaf forest, 35,907 pixels of oak-dominated deciduous broadleaf forest, 40,182 pixels of mixed forest (EN/DB), and 56,989 pixels of mixed forest (DN/DB). The seven forest types were combined into one forest layer in order to compare with the NLCD-1999/2000 dataset that does not differentiate forest types. The VGT-derived forest map was overlaid with the NLCD-1999/2000 dataset to determine the spatial agreement of forest pixels between these two datasets.

As the NLCD-1999/2000 dataset provides estimates forest cover within 1-km^2 pixels, the conventional pixel-based accuracy assessment (spatial agreement, commission error, omission error) will vary depending upon the threshold (%forest cover within 1-km pixels) used to define forest pixels in the NLCD dataset. For simplicity and illustrative purposes, we selected all NLCD pixels that have 1% or more fractional forest cover within 1-km^2 for pixel-based accuracy assessment. The use of a low definition of forest ($> 1\%$) from the NLCD dataset is likely to provide lower estimates of pixel-based accuracy assessment at 1-km resolution. According to the resultant map, 457,841 VGT-derived forest pixels correspond with those NLCD pixels that have 1% or more fractional cover of forest within 1-km^2 pixels. Thus, the pixel-based spatial agreement in forest pixels between the VGT-derived forest map (457,841) and NLCD-1999/2000 dataset (654,373) is about 70%. The pixel-based commission error is about 10% ($508{,}621 - 457{,}841 = 50{,}780$ pixels), while the pixel-based omission error is about 30% ($654{,}373 - 457{,}841 = 197{,}532$ pixels).

The area-weighted spatial agreement between the VGT-derived forest map and the NLCD-1999/2000 dataset should provide a more realistic and overall accuracy assessment, although it does not give estimates of commission and omission errors. The frequency distribution of VGT-derived forest pixels was calculated in reference to fractional cover of forest from the NLCD-1999/2000 dataset (Fig. 6). According to the histogram of VGT-derived forest pixels, 90% of the VGT-derived forest pixels (457,841) corresponds with those NLCD pixels that have a fractional forest cover of 30% or larger within 1-km pixels, and 75% of the VGT-derived forest pixels corresponds with those NLCD pixels that have a fractional forest cover of 60% or more (Fig. 6a). The cumulative area of forest for all the VGT forest pixels was calculated, using the fractional forest cover provided by the NLCD-1999/2000 dataset (Fig. 6b). The cumulative curves of forest area for both the NLCD pixels and VGT forest pixels are highly correlated (Fig. 6a). It is estimated that all the VGT forest pixels (457,841) cover a total forest area of 352,179 km^2, accounting for 83% of the total forest area (423,332 km^2) estimated by the NLCD-1999/2000 dataset, which is higher than the pixel-based spatial agreement (70%) between the NLCD pixels (654,373) and VGT forest pixels (457,841).

4.3. Characterization of seasonal dynamics of forests

Summary statistics of the NDVI and NDWI time series for all the seven forest types were calculated for characterization of seasonal dynamics of forest types (Fig. 7). The seasonal dynamics of NDVI time series (Fig. 7a) revealed only slight differences in NDVI values during the peak plant-growing season (July and August) among the seven forest types, but relatively large differences existed at the

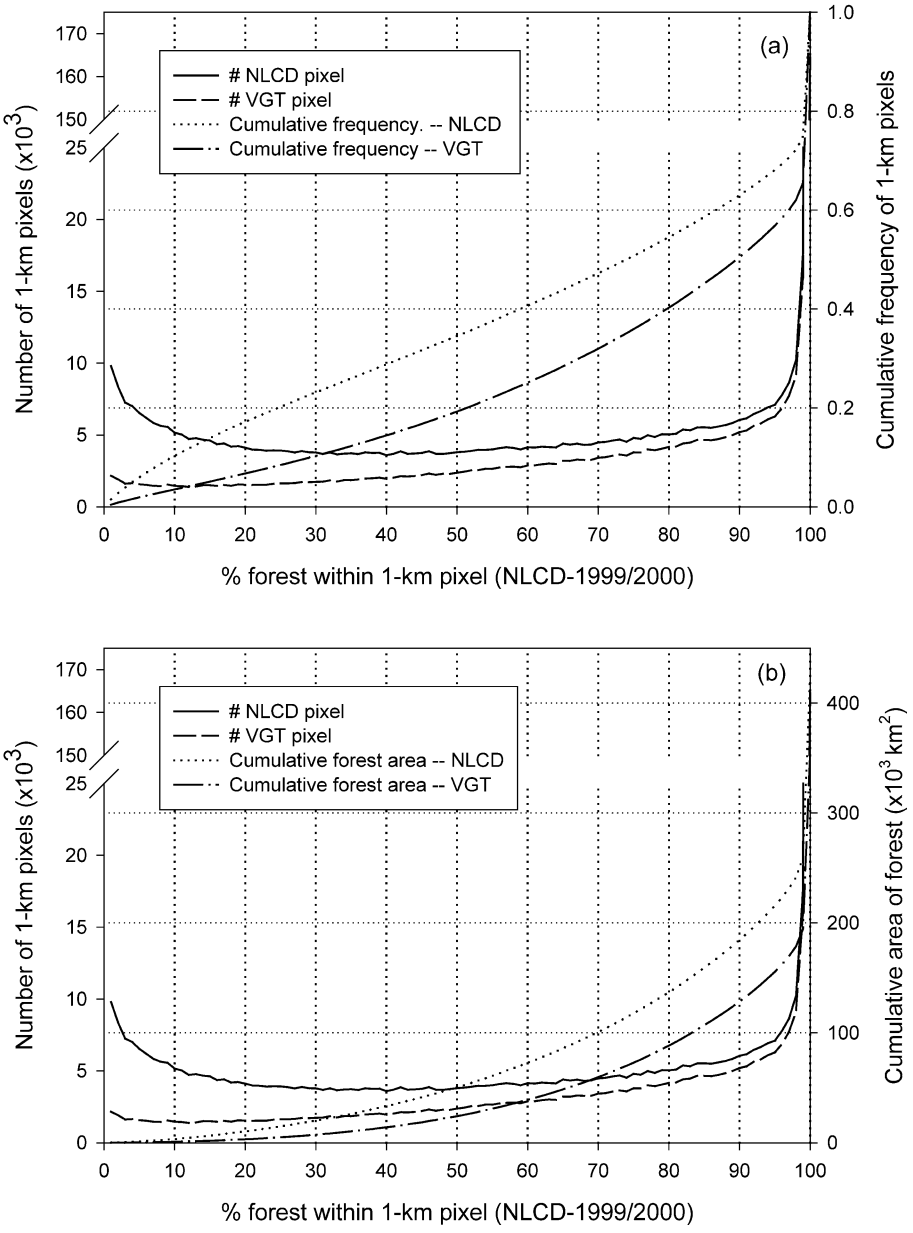

Fig. 6. Histograms of forest pixels from the NLCD-1999/2000 dataset and the VGT-derived forest map. (a) Number of pixels (pixel-based spatial agreement); and (b) area of forest (area-weighted spatial agreement).

beginning (March–April) and the end (October–November) of the study period. In March, evergreen needleleaf forest and the mixed forest with evergreen component (EN/DB) had the highest NDVI values (~ 0.20 and above), while deciduous needleleaf forest and deciduous broadleaf forests (DB-b, DB-m–b–b) had the lowest NDVI values (~ 0.10 and below). A seasonal NDVI development curve (Fig. 7a) is an indicator of greenness of vegetation, and has been widely used to define the starting point, ending point and length of plant growing seasons. Myneni, Tucker, Asrar, & Keeling (1998) used a threshold of 0.25 NDVI to define plant growing season in the northern latitudes. The deciduous forest types in our study area differed in the dates they surpassed and dropped below the 0.25 NDVI (Table 2). Using the 0.25 NDVI threshold, deciduous needleleaf forest and the mixed deciduous forest (DN/DB) have the shortest growing season (from April 21–30 to October 21–30), followed by birch-dominated deciduous broadleaf forest (DB-b, April 11–20 to October 21–30), maple–birch–basswood-dominated deciduous broadleaf forest (DB-m–b–b, April 11–20 to November 21–30) and oak-dominated deciduous broadleaf forest (DB-o, April 11–20 to November 21–30).

While the NDVI development curves of the seven forest types all have a bell shape (Fig. 7a), the seasonal dynamics of the NDWI time series have different shapes characterized by the "troughs" in the spring and fall seasons (Fig. 7b). The short-wave infrared (SWIR) band is sensitive to vege-

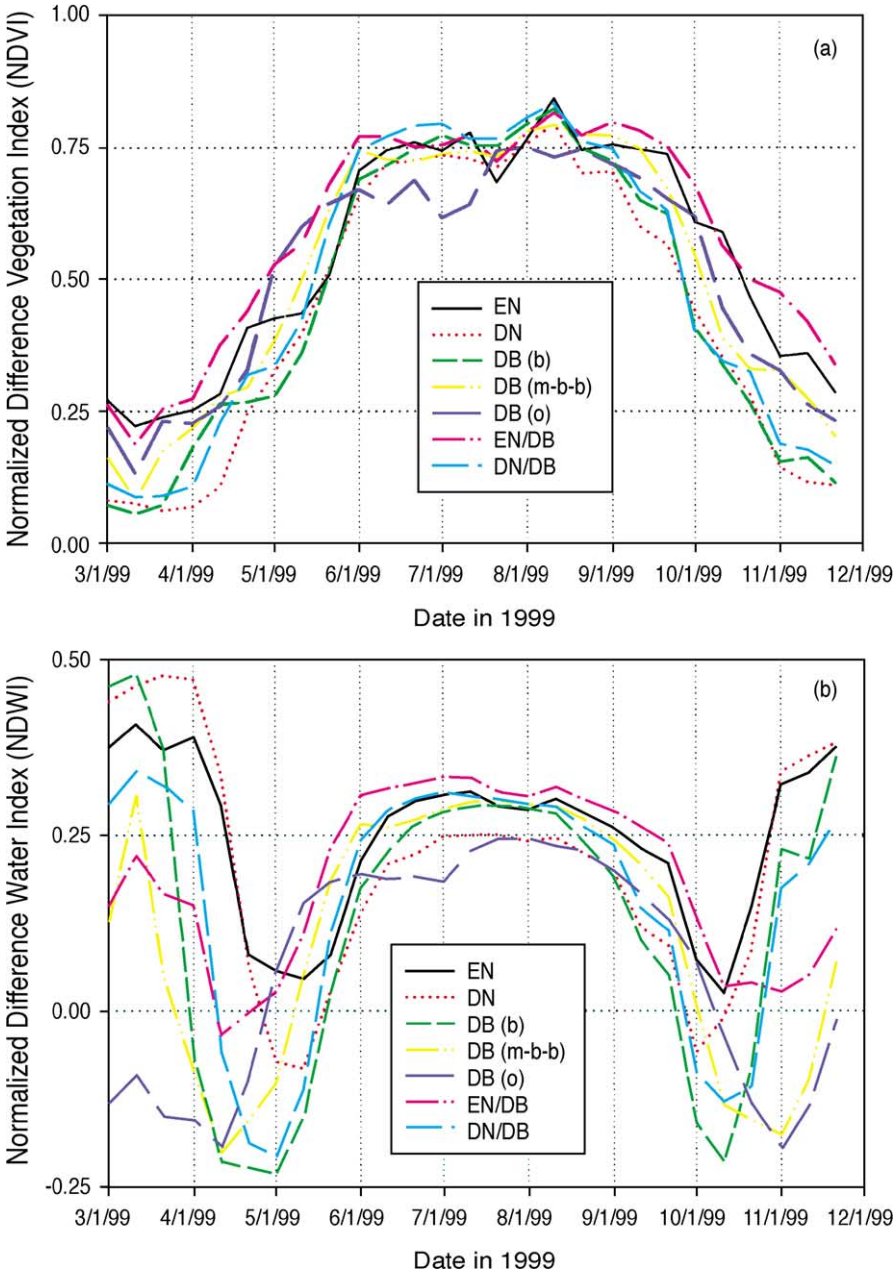

Fig. 7. Seasonal dynamics of mean NDVI (a) and NDWI (b) values over the period of March 1–10 to November 21–30, 1999 for the seven forest types in the study area.

tation cover, leaf moisture content and soil moisture. In mid-March, only oak-dominated deciduous broadleaf forest (DB-o) had negative NDWI values, while the other six forest types have positive NDWI values, mostly attributed to soil moisture from snow cover and melting snow water (Fig. 7b). The NDWI time series indicates that there were large differences between those forest types with evergreen needleleaf trees and those forest types with deciduous trees in mid-spring and mid-fall seasons (Fig. 7b). By late April to early May, most of the snow cover had melted, and NDWI values were positive and highest for evergreen needleleaf forest, but negative and lowest for the deciduous broadleaf forests (Fig. 7b). The observed difference in late spring NDWI values can be attributed to differences in leaf moisture content of the tree canopy between evergreen needleleaf species and deciduous broadleaf species. In late April to early May, evergreen needleleaf trees still have green leaves and abundant leaf water, and surface reflectance in the near-infrared (NIR) band is greater than surface reflectance in the SWIR band, resulting in positive NDWI values. By comparison, spring-time deciduous broadleaf trees have a mixed canopy of green leaves and woody plant material (which contains little water), with surface NIR reflectance less than SWIR reflectance, resulting in negative

Table 2
Dates of green-up process and senescence process of deciduous forests, according to the NDVI and NDWI thresholds from 10-day VGT composite data over the period of March 1–10, 1999 to November 21–30, 1999

Forest type	Green-up process in spring		Senescence process in fall	
	NDVI>0.25	NDWI>0.0	NDWI<0.0	NDVI<0.25
Deciduous needleleaf (DN)	4/21–30	5/21–30	10/1–10	11/1–10
Mixed forest (DN/DB)	4/21–30	5/21–30	10/1–10	11/1–10
Deciduous broadleaf (DB-b)	4/11–20	5/21–30	10/1–10	11/1–10
Deciduous broadleaf (DB-m–b–b)	4/11–20	5/11–20	10/11–20	11/21–30
Deciduous broadleaf (DB-o)	4/11–20	5/1–10	10/11–20	11/21–30

NDWI values. Similar patterns are also observed in October, when deciduous broadleaf trees began to experience senescence and losses of leaves (Fig. 7b). The NDWI time series also indicates that there were distinct differences between some of the deciduous broadleaf forest categories, specifically the oak-dominated and birch-dominated deciduous broadleaf forests (Fig. 7b). The oak-dominated broadleaf forests occur primarily in the southern part of the study area (Fig. 5) and are characteristic of the temperate mixed hardwood forest (Wang, 1961). Birch-dominated forests are characteristic of the boreal forest and are located in the northern portions of Inner Mongolia and Heilongjiang Provinces (Fig. 5). Deciduous broadleaf forest types differ in the first time that NDWI values were positive in the spring season and were negative in the fall season (Table 2).

Phenology of deciduous forest is characterized by green-up in spring and senescence in fall. In the spring, NDVI may indicate when the green-up process starts and NDWI may indicate when the green-up process ends, corresponding to an observable process from fully senescent to fully green vegetation canopy. In the fall, NDWI may indicate when the senescence process begins and NDVI may indicate when the senescence process ends, corresponding to an observable process from fully green to fully senescent vegetation canopy. The three types of deciduous broadleaf forests in our study area all exhibit unique green-up and senescence patterns (Table 2).

5. Discussion

The analyses of VGT-derived NDVI and NDWI data from March to November 1999 highlight significant seasonal differences among the various forest types in the study area. The VGT-derived NDVI time series is very useful for separating those forests that are dominated by evergreen tree species from forests that are dominated by deciduous tree species. This is consistent with earlier works that used AVHRR-derived NDVI time-series data for land cover mapping at large spatial scales (Tucker et al., 1985; Goward et al., 1985; Loveland et al., 1991, 2000; Zhu & Evans, 1994; Stone et al., 1994; Defries et al., 1995; Defries & Townshend, 1994; Liu et al., 1998; Hansen et al., 2000). VGT-derived NDWI time series provides additional and unique information on forest types and dynamics. Therefore, NDVI and NDWI time series complement each other and provide an improved and comprehensive description of forest types and phenology. Note that bi-directional reflectance distribution function (BRDF) of the land surface was not taken into consideration in pre-processing of VGT-S10 data, which may introduce some uncertainty in forest cover classification based on the VGT-S10 data. The BRDF can be used to compare observations obtained at different viewing angles or to standardize observations to a common geometry (Hu, Lucht, Li, & Strahler, 1997). Therefore, further studies are needed to incorporate the BRDF corrections into pre-processing of VGT-S10 data and to assess the effect of BRDF on forest cover characterization at large spatial scales.

We used both NDVI and NDWI time series to construct a general picture of phenology of forests in the study area. Previously, AVHRR-derived NDVI data have been used to define the length of temperate forest growing seasons, using NDVI threshold values ranging from 0.25 (Myneni et al., 1998) to 0.45 (Jenkins, Braswell, Frolking, & Aber, in press). The VGT-derived NDVI and NDWI time series suggest that the 0.25 NDVI threshold is appropriate for the onset of greenness development of deciduous forest types in northeastern China. In addition to information on starting and ending dates of plant growing season, it is important to quantify how long it takes for forests to complete the green-up process in spring and senescence process in fall. In this study, we proposed a NDVI- and NDWI-based scheme for quantifying the lengths of the green-up process in spring and the senescence process in fall. However, we have no field observation data from 1999 to test the hypothesis, and therefore, field studies are needed to measure forest canopy dynamics (proportions of senescent vegetation and green vegetation) over time in the spring and fall seasons. The 10-day composite data (VGT-S10) are generated by selection of those pixels of maximum NDVI values within a 10-day period. Using daily VGT data for phenological analysis would provide more accurate information on the dates of the green-up and senescence processes.

For forest classification using medium- to coarse-resolution images and the per-pixel binary approach, accuracy assessment of the resultant forest maps is critical and challenging due to the sub-pixel heterogeneity of the land surface (a mixture of tree, shrub, crop, soil, water, etc.). Accuracy assessment is usually done at three spatial scales: (1) field-based point survey data (micro-scale); (2) fine-resolution space-borne remotely sensed data (e.g. Landsat TM, SPOT and IKONOS) and/or aerial photos (medium scale) and (3) forest inventory data across large spatial domains (macro-scale). Field surveys require collection of

a large sample of field sites and are widely used for validation of TM-derived forest maps, however, they are usually constrained by limited resources and time. For validation of the AVHRR-derived global land cover dataset (IGBP DIScover), samples of Landsat TM- and SPOT-derived maps were used (Scepan, 1999; Scepan et al., 1999). In this study, we used the 1:100,000 scale land cover dataset derived from Landsat 7 ETM+ images acquired in 1999/2000 for validation, which is consistent in image acquisition time and spatial coverage with the VGT images we analyzed. Accuracy assessment of forest maps at medium- to coarse-spatial resolution is also affected by the legend of the classification scheme. For example, the Land Cover Classification Scheme developed by IGBP for global-scale land cover mapping is widely used, and includes five categories of forest: evergreen needleleaf forest, evergreen broadleaf forest, deciduous needleleaf forest, deciduous broadleaf forest and mixed forest. Its description for forest is "land dominated by trees with a percent canopy cover >60% and height exceeding 2 meters" (Scepan, 1999). For large-scale forest cover mapping, it is difficult to obtain estimates of percent tree canopy cover, and it requires a large sample of very-fine-resolution aerial photos or space-borne images (e.g. 1 or 4 m IKONOS). Landsat TM and ETM+ images at 30-m spatial resolution provide an alternative data source for estimating proportion of land cover types within 1-km pixels (Xiao et al., 2002a). In this study, the NLCD-1999/2000 dataset (1:100,000 scale) allows us to evaluate the VGT-derived forest map at a large spatial scale.

The results of this VGT image analysis demonstrate the potential of multi-temporal VGT images for identifying and mapping various forest types in temperate and boreal zones.

Dynamic monitoring of forests in northeast China must satisfy the following criteria: (a) timely data acquisitions (to detect the frequent disturbances that affect the study area), (b) spatially adequate (the spatial resolution must be sufficient to detect most of the disturbances that occur), (c) species sensitive (because carbon densities differ greatly among forest types). Although the NLCD-1999/2000 dataset provides a reliable estimate of total forested area, no details are provided regarding the type of forests present, due to the very low probability of acquiring multi-season cloud-free ETM+ images for a study area within 1 to 2 years. Therefore, an integrated mapping system that uses both multi-temporal medium- to coarse-resolution images (e.g. VGT and MODIS) and infrequent fine-resolution images (e.g. Landsat 7 ETM+) would have the potential to realize dynamic monitoring of forests across various spatial scales from landscape to the globe.

Acknowledgements

This study was supported by the NASA Earth Observing System (EOS) interdisciplinary science program (NAG5-6137, NAG5-10135), the NASA Terrestrial Ecology program (NAG5-7631), and the NASA Land Use and Land Cover Change program (NAG5-11160). We thank the three anonymous reviewers for their comments and suggestions on the earlier version of the manuscript.

References

Achard, F., Eva, H., & Mayaux, P. (2001). Tropical forest mapping from coarse spatial resolution satellite data: production and accuracy assessment issues. *International Journal of Remote Sensing*, *22*(14), 2741–2762.

Barnes, B. V., Xu, Z., & Zhao, S. (1992). Forest ecosystems in an old-growth pine-mixed hardwood forest of the Changbai Shan Preserve in Northeastern China. *Canadian Journal of Forest Research*, *22*, 144–160.

Burger, D., & Zhao, S. (1988). An introductory comparison of forest ecological conditions in Northeastern China and Ontario, Canada. *Forestry Chronicle*, *64*, 105–115.

Chen, X. (2000). Characteristic change of several forest landscapes between 1896 and 1986 in Heilongjiang Province. *Acta Botanica Sinica*, *42*, 979–984.

Chen, X., Zhang, X., Zhou, G., & Chen, J. (2000). Spatial characteristics and change for tree species (genera) along Northeast China Transect. *Acta Botanica Sinica*, *42*, 1075–1081.

Cihlar, J., Xiao, Q., Chen, J., Beaubien, J., Fung, K., & Latifovic, R. (1998). Classification by progressive generalization: a new automated methodology for remote sensing multichannel data. *International Journal of Remote Sensing*, *19*, 2685–2704.

Defries, R., Hansen, M., & Townshend, J. (1995). Global discrimination of land cover types from metrics derived from AVHRR Pathfinder data. *Remote Sensing of Environment*, *54*, 209–222.

Defries, R., & Townshend, J. (1994). NDVI-derived land classifications at a global scale. *International Journal of Remote Sensing*, *17*, 3567–3586.

ECAFC (The Editorial Committee for the Atlas of Forestry in China) (1990). The Atlas of Forestry in China. Beijing, China: Press of Map and Survey, 389 pp. (in Chinese).

Fang, J., Chen, A., Peng, C., Zhao, S., & Ci, L. (2001). Changes in forest biomass carbon storage in China Between 1949 and 1998. *Science*, *292*, 2320–2322.

Fang, J., Wang, G., Liu, G., & Xu, S. (1998). Forest biomass of China: an estimate based on the biomass–volume relationship. *Ecological Applications*, *8*, 1084–1091.

Gao, B. (1996). NDWI—a normalized difference water index for remote sensing of vegetation liquid water from space. *Remote Sensing of Environment*, *58*, 257–266.

Geng, X., Pastor, J., & Dewey, B. (1993). Decay and nitrogen dynamics of litter from disjunct, congeneric tree species in old-growth stands in northeastern China and Wisconsin. *Canadian Journal of Botany*, *71*, 693–699.

Goward, S. N., Tucker, C. J., & Dye, D. G. (1985). North American vegetation patterns observed with the NOAA-7 advanced very high resolution radiometer. *Vegetatio*, *64*, 3–14.

Hansen, M. C., DeFries, R. S., Townshend, J. R. G., & Sohlberg, R. (2000). Global land cover classification at 1 km resolution using a classification tree approach. *International Journal of Remote Sensing*, *6/7*, 1331–1364.

Hu, B., Lucht, W., Li, X., & Strahler, A. H. (1997). Validation of kernel-driven semiempirical models for the surface bi-directional reflectance distribution function of land surface. *Remote Sensing of Environment*, *62*, 201–214.

Jenkins, J. P., Braswell, B. H., Frolking, S. E., & Aber, J. A. (2001). Predicting spatial and interannual patterns of temperate forest springtime phenology in the eastern U.S. *Geophysical Research Letters* (in press).

Jiang, H., Apps, M. J., Zhang, Y., Peng, C., & Woodard, P. (1999). Modelling the spatial pattern of net primary productivity in Chinese forests. *Ecological Modelling*, *122*, 275–288.

Jiang, H., Peng, C., Apps, M. J., Zhang, Y., Woodard, P., & Wang, Z. (1999). Modelling the net primary productivity of temperate forest ecosystems in China with a GAP model. *Ecological Modelling*, *122*, 225–238.

Jürgens, C. (1997). The modified normalized difference vegetation index (mNDVI)—a new index to determine frost damages in agriculture based on Landsat TM data. *International Journal of Remote Sensing*, *18*, 3583–3594.

Liu, J., Zhuang, D., & Ling, Y. (1998). Vegetation integrated classification and mapping using remote sensing and GIS techniques in Northeast China. *Journal of Remote Sensing*, *4*, 285–291 (in Chinese).

Liu, J., Zhuang, D., Lou, D., & Xiao, X. (2001). Land-cover classification of China: integrated analysis of AVHRR imagery and geo-physical data. *International Journal of Remote Sensing* (accepted subject to revision).

Liu, Q., Kondoh, A., Tateishi, R., Takamura, T., & Takeuchi, N. (2001). Monitoring of the stability of boreal forest ecosystem in Northeast China in relation with natural disturbance by Landsat TM imagery. In W. L. Smith, & Y. Yasouka (Eds.), Hyperspectral Remote Sensing of the Land and Atmosphere. *Proceedings of SPIE, vol. 4151* (pp. 222–230).

Loveland, T. R., Merchant, J. W., & Brown, J. F. (1991). Development of a land-cover characteristics database for the conterminous U.S. *Photogrammetric Engineering & Remote Sensing*, *11*, 1453–1463.

Loveland, T. R., Reed, B. C., Brown, J. F., Ohlen, D. O., Zhu, Z., Yang, L., & Merchant, J. W. (2000). Development of a global land cover characteristics database and IGBP DIScover from 1-km AVHRR data. *International Journal of Remote Sensing*, *6/7*, 1303–1330.

Mayaux, P., Gond, V., & Bartholome, E. (2000). A near-real time forest cover map of Madagascar derived from SPOT-4 VEGETATION (VGT) data. *International Journal of Remote Sensing*, *16*, 3139–3144.

Mayaux, P., & Lambin, E. F. (1997). Tropical forest area measured from global land cover classifications: inverse calibration models based on spatial textures. *Remote Sensing of Environment*, *59*, 29–43.

Ministry of Forestry, People's Republic of China (1990). National Forestry Statistics (1949–1987). Beijing: China's Forestry Press.

Ministry of Forestry, People's Republic of China (1996). The National Census of Forest Resources (1989–1993). Beijing: China's Forestry Press.

Myneni, R. B., Tucker, C. J., Asrar, G., & Keeling, C. D. (1998). Interannual variations in satellite-sensed vegetation index data from 1981 to 1991. *J. Geophys. Res.*, *103*(D6), 6145–6160.

Rahman, H., & Dedieu, G. (1994). SMAC: a simplified method for atmospheric correction of satellite measurements in the solar spectrum. *International Journal of Remote Sensing*, *15*, 123–143.

Reed, B., Brown, J., VanderZee, D., Loveland, T., Merchant, J., & Ohlen, D. (1994). Measured phenological variability from satellite imagery. *Journal of Vegetation Science*, *5*, 703–714.

Richardson, S. D. (1990). *Forests and Forestry in China*. Washington: Island Press.

Saint, G. (2000). Proceedings of VEGETATION 2000: 2 years of operation to prepare the future. International Conference of VEGETATION 2000, April 3–6, Lake Maggiore, Italy.

Scepan, J. (1999). Thematic validation of high-resolution global land-cover data sets. *Photogrammetric Engineering & Remote Sensing*, *65*, 1051–1060.

Scepan, J., Menz, G., & Hansen, M. C. (1999). The DIScover validation image interpretation process. *Photogrammetric Engineering & Remote Sensing*, *65*, 1075–1081.

Schimel, D. S., House, J. I., Hibbard, K. A., Bousqet, P., Ciais, P., Peylin, P., Braswell, B. H., Apps, M. J., Baker, D., Bondeau, A., Canadell, J., Churkina, G., Cramer, W., Denning, A. S., Field, C. B., Friedlingstein, P., Goodale, C., Heimann, M., Houghton, R. A., Melillo, J. M., Moore, III, B., Murdiyarso, D., Noble, I., Pacala, S. W., Prentice, I. C., Raupach, M. R., Rayner, P. J., Scholes, R. J., Steffen, W. L., & Wirth, C. (2001). Recent patterns and mechanisms of carbon exchange by terrestrial ecosystems. *Nature*, *414*, 169–172.

Shao, G., Zhao, G., Zhao, S., Shugart, H. H., Wang, S., & Schaller, J. (1996). Forest cover types derived from Landsat Thematic Mapper Imagery for Changbai Mountain area of China. *Canadian Journal of Forest Research*, *26*, 206–216.

Stone, T., Schlesinger, P., Houghton, R. A., & Woodwell, G. M. (1994). A map of the vegetation of South America based on satellite imagery. *Photogrammetric Engineering & Remote Sensing*, *5*, 541–551.

Tang, X. (2000). Studies on geo-spatial data fusion and its applications. PhD Dissertation, Institute of Remote Sensing Applications, Chinese Academy of Sciences, Beijing, China, 139 pp. (in Chinese).

Tucker, C. J. (1980). Remote sensing of leaf water content in the near-infrared. *Remote Sensing of Environment*, *10*, 23–32.

Tucker, C. J., Townshend, J. R. G., & Goff, T. E. (1985). African land cover classification using satellite data. *Science*, *4685*, 369–375.

Viovy, N., Arino, O., & Belward, A. S. (1992). The Best Index Slope Extraction (BISE): a method for reducing noise in NDVI time-series. *International Journal of Remote Sensing*, *8*, 1585–1590.

Wang, C. (1961). *The Forests of China.* Maria Moors Cabot Foundation Publication Series, vol. 5. Cambridge, MA: Harvard University.

Wang, X., Feng, Z., & Ouyang, Z. (2001). The impact of human disturbance on vegetative carbon storage in forest ecosystems in China. *Forest Ecology and Management*, *148*, 117–123.

White, M., Thornton, P., & Running, S. (1997). A continental phenology model for monitoring vegetation responses to interannual climatic variability. *Global Biogeochemical Cycles*, *11*, 217–234.

Wu, C. (1990). Land-use map of China (1:1,000,000). Beijing: Science Press.

Xiao, X., Boles, S., Frolking, S., Salas, W., Moore, B., Li, C., He, L., & Zhao, R. (2002a). Landscape-scale characterization of cropland in China using VEGETATION sensor data and Landsat TM imagery. *International Journal of Remote Sensing* (in press).

Xiao, X., Boles, S., Frolking, S., Salas, W., Moore, B., Li, C., He, L., & Zhao, R. (2002b). Observation of flooding and rice transplanting of paddy rice fields at the site to landscape scales in China using VEGETATION sensor data. *International Journal of Remote Sensing* (in press).

Xiao, X., Moore, B., Qin, X., Shen, Z., & Boles, S. (2002). Large-scale observation of alpine snow and ice cover in Asia: using multi-temporal VEGETATION sensor data. *International Journal of Remote Sensing*, *23*, 2213–2228.

Xiao, X., Shen, Z., & Qin, X. (2001). Assessing the potential of VEGETATION sensor data for mapping snow and ice cover: a normalized difference snow and ice index. *International Journal of Remote Sensing*, *22*, 2479–2487.

Zheng, D., Wallin, D. O., & Hao, Z. (1997). Rates and patterns of landscape change between l972 and 1988 in the Changbai Mountain area in China and North Korea. *Landscape Ecology*, *12*, 241–254.

Zheng, Y., Xiao, X., Guo, Z., & Howard, T. (2001). A county-level analysis of the spatial distribution of forest resources in China. *Journal of Forest Planning*, *7*, 69–78.

Zhu, Z., & Evans, D. L. (1994). U.S. forest types and predicted percent forest cover from AVHRR data. *Photogrammetric Engineering & Remote Sensing*, *5*, 525–531.